Article

Cu/CuOx@C Composite as a High-Efficiency Electrocatalyst for Oxygen Reduction Reactions

Ding Zhang [1], Yun-Fei Li [2], Li-Xue Liu [1], Lei Duan [2], Zhi-Li Ren [2], Shou-Dong Xu [2], Liang Chen [2,*], Hui-Juan Guo [1], Yi Huang [1], Li-Juan Shi [1] and Qun Yi [1,*]

[1] School of Chemical Engineering and Pharmacy, Wuhan Institute of Technology, Wuhan 430205, China
[2] College of Chemical Engineering, Taiyuan University of Technology, Taiyuan 030024, China
* Correspondence: chenliang@tyut.edu.cn (L.C.); yq20210901@wit.edu.cn (Q.Y.); Tel.: +86-351-6018554 (L.C.); +86-27-87194980 (Q.Y.)

Abstract: Among clean energy transformation devices, fuel cells have gained special attention over the past years; however, advancing appropriate non-valuable metal impetuses to halfway supplant the customary Pt/C impetus is still in progress. In this paper, we propose a specific electrocatalyst in the formula of highly-active Cu species, associated with coated carbon (Cu@C-800), for oxygen reduction reaction (ORR) through post-treatment of a self-assembled precursor. The optimized catalyst Cu@C-800 showed excellent ORR performance (i.e., the onset potential was 1.00 V vs. RHE, and half-wave potential of 0.81 V vs. RHE), high stability, resistance to methanol, and high four-electron selectivity. The enhancement is attributed to the synergy between the carbon matrix and a high explicit surface region and rich Cu nano-species.

Keywords: oxygen reduction reaction (ORR); electrocatalyst; self-assembly; one-dimensional; Cu-based

1. Introduction

Meeting the ever-increasing energy demand with lower carbon production and clean output is considered as one of the essential issues for human society sustainability. This requires advancing the clean energy transformation frameworks [1,2]. The power devices can change compound energy into power. The most common application is transforming hydrogen into electricity to power automobiles or fixed equipment [3,4].

In developing high-performance fuel cells, the oxygen reduction reaction occurs on cathode surfaces [5]. It is reported that platinum and its derivatives, such as the composite Pt/C, exhibit excellent electrocatalytic activity for ORR [6]. However, platinum-based catalysts are usually expensive, intolerant to methanol, and sensitive to carbon monoxide poisoning. Therefore, researchers are seeking other promising electrocatalysts such as carbon-based metal-free catalysts [7,8], metal oxide catalysts [9], and carbon/non-precious metal catalysts (NPMCs) [10–12].

It is believed that the ORR action of carbon-based NPMCs is powerless to the metal species since the dynamic community and ordinarily follows the request for Fe > Co > Mn > Cu > Cr > Ni > Zn ≈ without metal [13]. Moreover, various iron, cobalt, and iron–cobalt alloy catalysts have been proposed with the tuning of chemical formula, micro-morphology, and local coordination structure [14,15], some of which show significantly greater reactant execution than the commercial Pt/C under soluble circumstances [16–19]. However, the intensively explored Fe–N–C catalysts often show limited stability caused by the Fenton effect [20]. In contrast, the Co–N–C catalyst shows an alleviated Fenton reaction, as Co-based active sites show weaker intrinsic ORR activity and produce less H_2O_2 [21]. In addition, copper has been investigated as an electrocatalyst for the ORR process considering its second-greatest conductivity (after silver), low price, and bountiful storage [22].

The Cu-based ORR catalysts, such as Cu/Zn synergistic single-atom catalyst Cu/Zn-NC, with excellent catalytic performance, were prepared using the ZIF-8 precursor [23]. For instance, a large Cu was converted into an isolated Cu single atom using a gas migration strategy [24], and anchored to the N-doped carbon received from ZIF-8 to set up an effective Cu-NC impetus, based on ZIF-67 precursor prepared by N-rich mesoporous carbon-supported Cu-based ORR electrocatalyst [25]. Guo et al. reported on the ORR electrocatalytic activity of Cu/rGO nanocomposites and their effects on methanol and CO [26]. Although these catalysts exhibited excellent electrocatalytic performance, there were limitations due to the high preparation cost and low yield associated with limitation of their raw materials.

In this paper, we present a straightforward union of 1D Cu/CuO$_x$@C nanofibers, for which a graphite carbon shell encapsulates the dispersed copper/copper oxide nanoparticles (Cu/CuO$_x$ NPs). This was obtained through underlying pyrolysis of natural layered copper hydroxide, Cu(OH)(Hsal)·H$_2$O, as the template and precursor to generate intermediate material, Cu@C, followed by chemical etching and secondary pyrolysis to obtain the final material, i.e., Cu/CuOx@C. The resulting catalyst showed accelerated ORR activity ($E_{1/2}$ is 0.81 V vs. RHE, and J_L is 5.15 mA/cm^2), four-electron selectivity, and excellent resistance to methanol.

2. Results

2.1. Synthesis and Characterization

In Figure 1, the synthesis procedure of the target material, Cu@C-800, is illustrated. Uniform 1D Cu(OH)(Hsal)·H$_2$O as an organic layered metal salt (LHSs) was prepared via mixing of hydrated copper nitrate and sodium salicylate (NaHsal) and initiating the self-assembly at certain pH. Here, Hsal stands for *o*-HOC$_6$H$_4$COO$^-$. The obtained Cu(OH)(Hsal)·H$_2$O was pyrolyzed to obtain Cu@C nanofibers [27] and further chemically etched by FeCl$_3$ solution. Finally, it was pyrolyzed again to obtain the final product, Cu@C-800. The other electrocatalyst samples (Cu@C-600, Cu@C-700, and Cu@C-900) were similarly prepared by varying the final pyrolysis temperature.
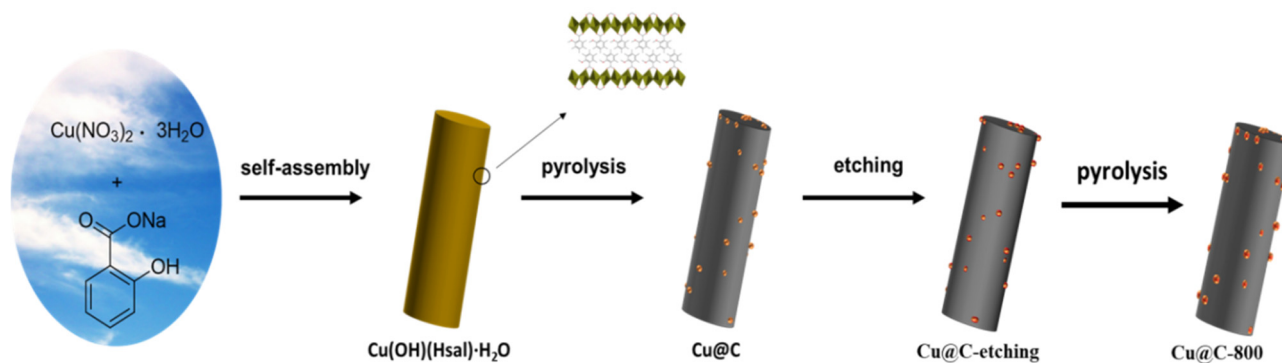

Figure 1. Cu@C-800 synthesis strategy.

The wide-angle X-ray powder diffraction pattern of Cu@C in Figure 2a shows articulated diffraction tops situated at 2θ = 43.2°, 50.4°and 74.1°, highlighting the (111), (200), and (220) planes for Cu (JCPDS:65-9743), which are consistent with the previous literature [28,29]. After FeCl$_3$ etching, the observed diffraction peaks are located at 2θ = 29.5°, 36.4°, 42.2°, 61.3°, 73.5°, 77.3°, and 92.4°, indexed by the cubic fcc structure of Cu$_{2+1}$O, which are consistent with the Cu$_{2+1}$O prepared by other techniques [30,31]. The diffraction pinnacles of Cu@C-800 are seen at 2θ = 43.2°, 50.4°, and 74.1°, which highlight the (111), (200), and (220) planes of the cubic copper. Thus, the evolution of Cu species can be described as the oxidation of Cu to Cu$_{2+1}$O, followed by subsequent reduction to Cu.
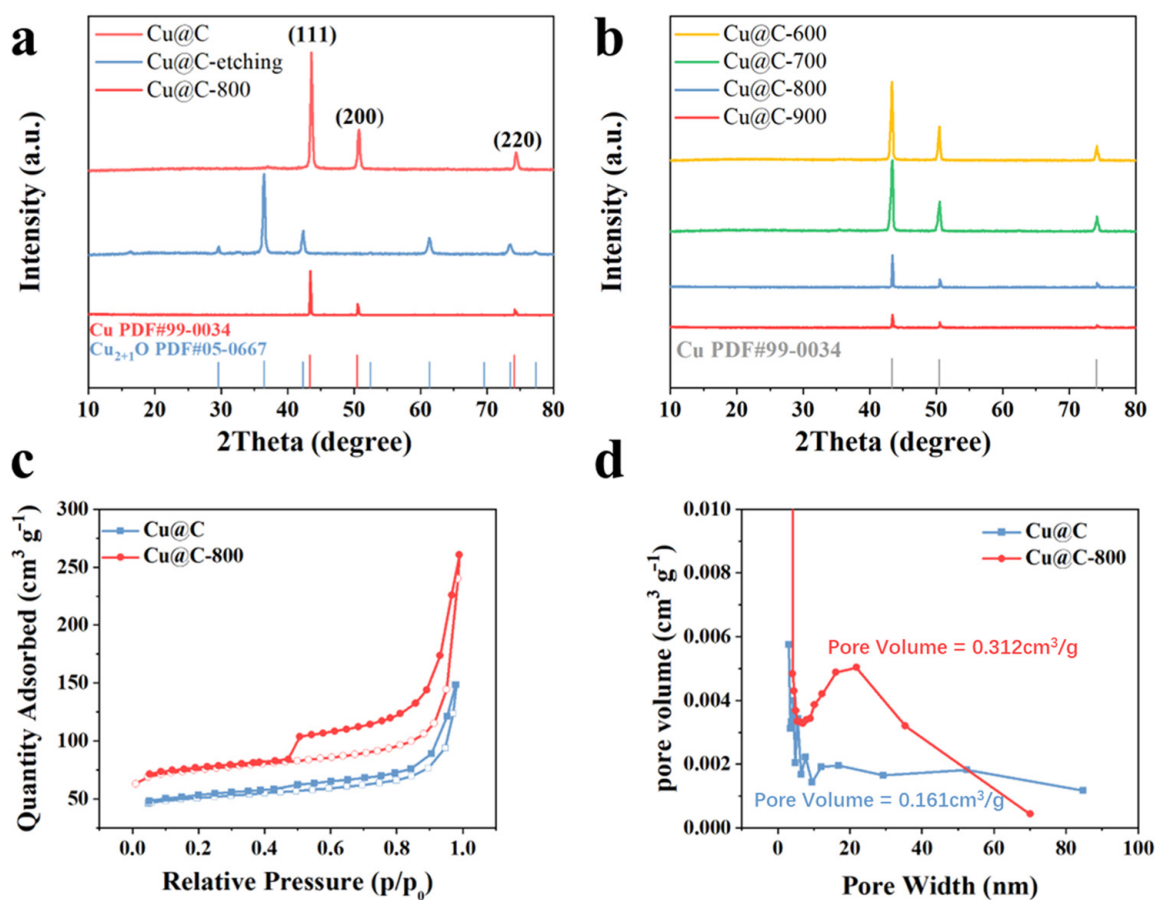
Figure 2. (**a**) XRD of Cu@C, Cu@C-etching, Cu@C-800; (**b**) XRD of Cu@C-(600, 700, 800, 900); Nitrogen adsorption–desorption isotherm of (**c**) Cu@C-800 and Cu@C; Pore size distribution of (**d**) Cu@C-800 and Cu@C.

As shown in Figure 2b, XRD analysis of Cu@C-600, Cu@C-700, Cu@C-800, and Cu@C-900 shows pronounced, highly-crystalline Cu NPs diffraction peaks, which are located at $2\theta = 43.2°$, $50.4°$, and $74.1°$, respectively. Moreover, it is concluded that the crystalline grain size for the final Cu/C samples gradually increased by increasing the secondary pyrolysis temperature through estimating the half peak width of (111) peaks (Table S1).

The nitrogen adsorption and desorption curves of Cu@C-800 and Cu@C are shown in Figure 2c,d. The calculated specific surface areas, average pore diameters and pore volumes of Cu@C-800 and Cu@C are 286 m^2 g^{-1} and 197 m^2 g^{-1}, 12–20 nm and 3–4 nm, and 0.31 cm^3/g and 0.16 cm^3/g, respectively. The presence of mesopores ensured adequate contact of electrolytes and reactants with the active center on the catalyst surface [32]. Carbon rods provided a large specific surface area and electronic conductivity, which favored the charge transfer process for the electrocatalysts [33].

The SEM and TEM images of the precursors, Cu@C, Cu@C-etching, and Cu@C-800, are shown in Figure 3a–d and Figure S1, respectively. A homogeneous precursor Cu(OH)(Hsal)·H$_2$O was obtained by self-gathering of copper nitrate trihydrate and sodium salicylate (NaHsal) (Figure 3a), and its XRD pattern shown in Figure S2 indicates a typical layered structure [27]. Moreover, the diameter of Cu(OH)(Hsal)·H$_2$O was about 200 nm and tended to aggregate into bundles. As shown in the TEM image, the prepared Cu@C maintained the nanorods' morphology, but the active site Cu showed up as circular Cu nanoparticles with an average size of 78 nm conveyed on the nanorods (Figure S3).
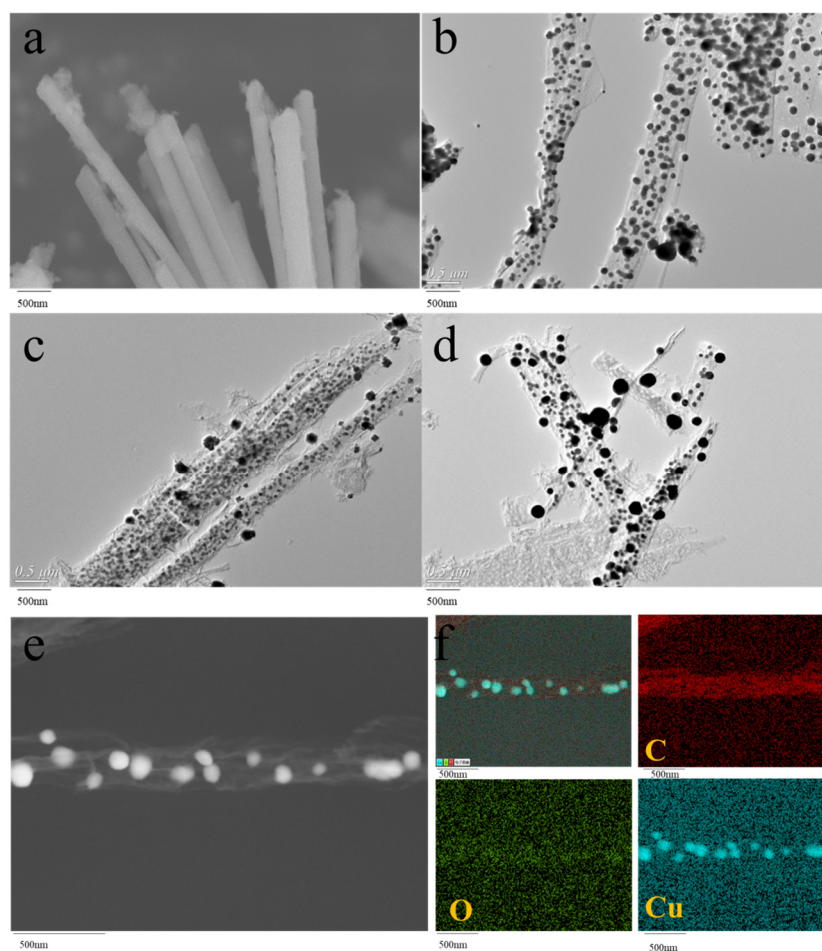
Figure 3. SEM and TEM images for the precursor and catalyst samples; SEM: (**a**) Cu(OH)(Hsal)·H_2O; TEM: (**b**) Cu@C, (**c**) Cu@C-etching, (**d**) Cu@C-800; (**e**) TEM picture of Cu@C-800; (**f**) EDS element distribution map for the sample Cu@C-800.

We used a high-resolution scanning electron microscope to study the Cu@C-800 sample (Figure 3e), which showed a clear rod-like morphology. The splendid spots on the SEM pictures were credited to the arbitrarily disseminated nano-sized Cu species on the carbon nanorods. The element distribution of Cu@C-800 displayed in Figure 3f indicates the atomic percentage of C (85.81%), O (7.26%), and Cu (6.92%), which further indicates the randomly anchored Cu/CuOx NPs on the carbon nanorods, illustrating that Cu was bonded to O in the form of catalytic sites.

The Raman response is also shown in Figure S4a, which shows two conspicuous peaks at 1334 and 1594 cm^{-1} for Cu@C-800, individually, compared to the D (cluttered) and G (requested) groups of carbon. The D band is attributed to disordered structure and defects in graphene, whereas the G band originates from the C-C stretching mode of sp^2-bonded carbon. The I_D/I_G value of Cu@C-800 is 1.01, indicating that it has more defective graphite structures and will expose more accessible oxygen-containing groups, which improves the ORR electrocatalytic activity [34,35].

The peaks at 312, 354, and 621 cm^{-1} in Figure S4b indicate the presence of CuO [36–39], and the peak at 519 cm^{-1} indicates the presence of Cu_2O [40–42]. Fourier infrared spectroscopy (*IR*) analysis shown in Figure S4c,d indicates the O–H bond's tensile vibration and bending vibration at 3440 cm^{-1} and 1617 cm^{-1}, respectively [43]. Furthermore, the peak at 1083 cm^{-1} is derived from the C–O bond [13], and the peaks at 605, 525, and 458 cm^{-1} are assigned to the vibrational stretching of the Cu–O bond [40,43–45].

In Figure 4, the XPS survey of Cu@C-800 and the spectra of C, Cu, and O are shown. The full spectrum confirms the coexistence of the three primary surface elements of C, O,

and Cu (Figure 4a), which are consistent with the characterization analysis discussed in HR-SEM section.
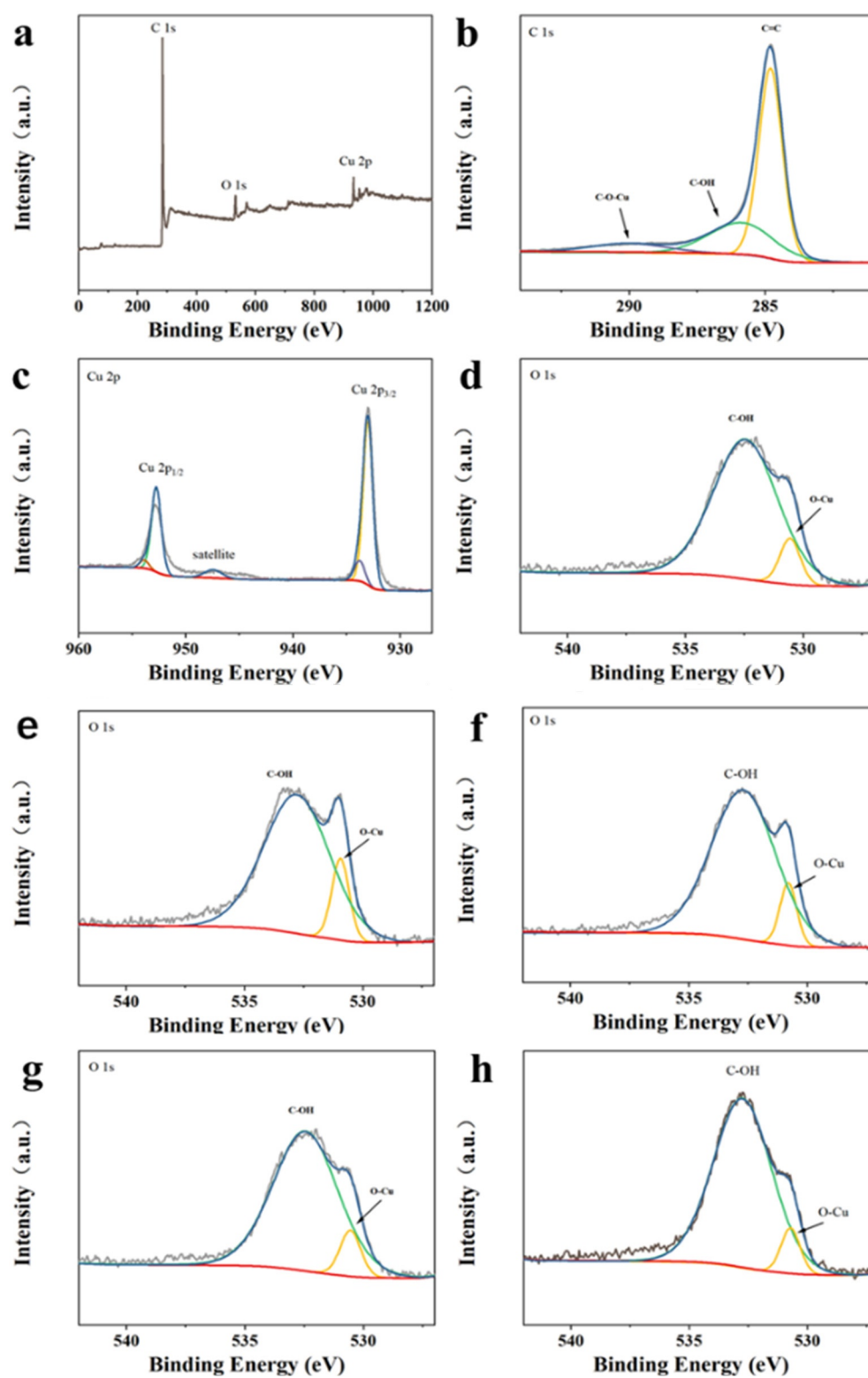

Figure 4. XPS of Cu@C-800 (**a**) full spectrum, (**b**) fine spectrum of C1s, (**c**) fine spectrum of Cu 2p, (**d**) fine spectrum of O1s, the O XPS fine spectrum of (**e**) Cu@C-600, (**f**) Cu@C-700, (**g**) Cu@C-800, (**h**) Cu@C-900.

In Figure 4b,c, the C and Cu's XPS fine spectrum are displayed. In Figure 4b, the C1s fine spectrum of Cu@C-800 is shown, and three peaks correspond to C=C (284.8 eV), C–OH (285.9 eV), and C–O–Cu (290 eV), which originate from the benzene ring of the Cu(OH)(Hsal)·H$_2$O. Moreover, the metallic Cu and Cu$^+$ (cuprous) are challenging to recognize by Cu 2p orbitals because their characteristic peaks appear in close positions (Figure 4c) [46]. The limiting energy tops at 932.7 eV and 952.5 eV are credited to the twist circle twofold pinnacles and energy level changes of Cu/Cu$^+$ 2p (Cu 2p$_{3/2}$ and Cu 2p$_{1/2}$) individually, respectively [47]. In addition, combined with the Raman characterization of Cu@C-800 in Figure 4Sb above, the top at 933.3 eV demonstrates the presence of divalent copper oxide CuO in the Cu@C-800 [46].

Further information about the O1s spectra can be achieved from Figure 4d to study the coordination effect between the C layer and the Cu surface in Cu@C-800. There are two satellite peaks at 530.6 eV (O–Cu) and 532.4 eV (C–OH), which indicate that the stable presence of Cu (I) may be attributed to the electron transfer between the Cu surface and C layer [27].

To clarify the effect of the secondary pyrolysis process on the surface profiles, O XPS fine spectrum analysis is performed on the samples, including Cu@C-600, Cu@C-700, Cu@C-800, and Cu@C-900. The corresponding fine spectrum of Cu is shown in Figure S5, and the ratio of the C–OH and O–Cu is reported in Table S1. These results confirmed that the proportion of O–Cu gradually decreased with the increase of the secondary pyrolysis temperature.

2.2. Electrocatalytic Performance

The cyclic voltammograms (CVs) of the Cu@C-800 under N$_2$ and O$_2$ saturation conditions are given in Figure 5a. A couple of irreversible redox tops are seen around 0.6 V (vs. RHE), which were ascribed to the redox cycle of Cu(I)/Cu(II) in a wet N$_2$ gas flow [48,49]. In contrast, it has an optimal electrocatalytic activity for ORR under the O$_2$ atmosphere, as the oxidation peak and the reduction peak current both increase significantly, and the peak potential is shifted at ≈ 0.76 V (vs. RHE).

The redox activity can be confirmed in the electrochemical test with different parameters, such as calculated electron transfer numbers (*n*) and optimal starting and half-wave potential. Firstly, we calculated the number of transferred electrons of Cu@C-800 by the *Koutecky-Levich* (*K-L*) equation. The sample Cu@C-800 shows a consistent slope, indicating the first-order reaction kinetics related to the oxygen concentration in the electrolyte [50,51]. Furthermore, the calculated electron transfer numbers (*n*) of Cu@C-800 at 0.2 V, 0.3 V, 0.4 V, and 0.5 V are 3.94, 3.92, 3.87, and 3.80, respectively, which confirm that the reaction follows the four-electron transfer pathway.

In the high-potential environment, Cu@C shows limited performance. However, the materials obtained by further treatment have shown greater stability and electrocatalytic activity. It is observed that Cu@C-800 shows an optimal starting potential E_{onset} (1.00 V vs. RHE) and a half-wave potential $E_{1/2}$ (0.81 V vs. RHE), and the greatest limiting diffusion current density (5.15 mA cm^{-2}) (Figure 5d–f). Moreover, the calculated Tafel slope of Cu@C-800 is 107 mV dec^{-1} (Figure 5g). Such activity can be mainly attributed to a high specific surface area and mesopore distribution, evidenced by nitrogen adsorption-desorption, favoring O$_2$ diffusion. Table S2 considers the ORR electrocatalytic boundaries of different agent Cu-based electrocatalysts announced in an antacid medium (0.1 M KOH). The catalytic activity of Cu@C-800 is comparable to the best catalysts for ORR [52–55].

In the electrolyte saturated with O$_2$, Cu@C-800 has shown a greater half-wave potential, indicating a good oxygen reduction activity (Figure 5b). For comparison, the examples of Cu@C-600, Cu@C-700, and Cu@C-900 were measured under similar circumstances, showing typical redox reactions (Figure S7) and dynamic current density at 0.81 V vs. RHE (Figure S8). We also calculated the number of transferred electrons for Cu@C-600, Cu@C-700, and Cu@C-900 (Figure S9) and found that the *n* value of Cu@C-800 and Cu@C-900 is

significantly greater than those of Cu@C-600 and Cu@C-700, but all the calculated n values confirms the four-electron process.
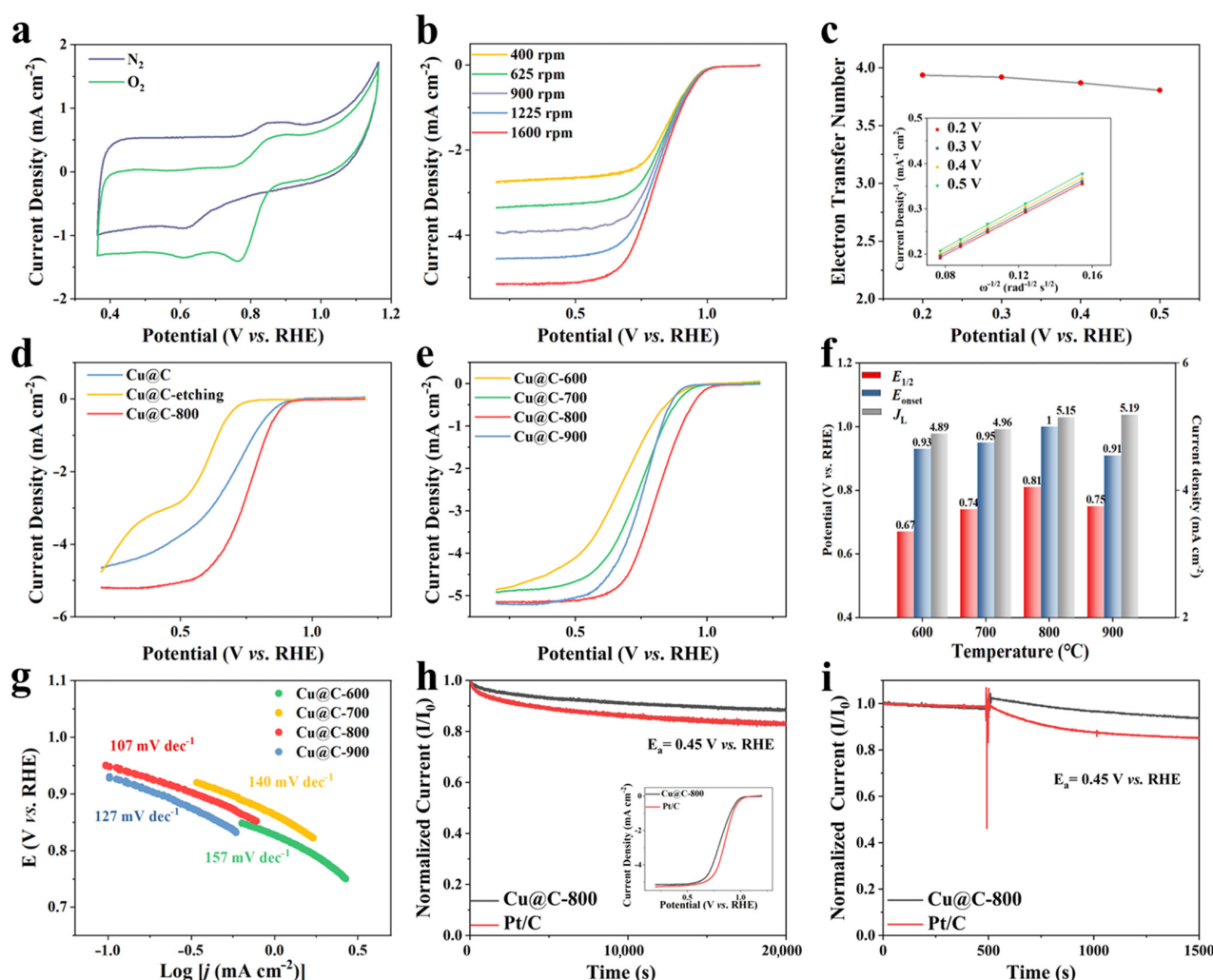

Figure 5. Cu@C-800 (**a**) CV, (**b**) LSV at different speeds, (**c**) electron transfer number 1600 rpm under O_2 saturation (**d**) LSV of Cu@C, Cu@C-etching, Cu@C-800 (**e**) LSV of Cu@C-(600, 700, 800 and 900) (**f**) Cu@C-(600, 700, 800 and 900) E_{onset}, $E_{1/2}$, JL. (**g**) The Tafel slope of Cu@C-(600, 700, 800 and 900); (**h**) stability test of Cu@C-800 and Pt/C and (**i**) methanol resistance test of Cu@C-800 and Pt/C.

The oxygen reduction reaction in the aqueous alkaline medium (0.1 M KOH) involved several oxygen-containing intermediates participating in the multi-step reaction. There are two possible pathways in alkaline solutions for the four-electron ORR process, namely dissociation and binding mechanisms (Figure S10). Irrespective of the dissociation or binding mechanisms, the ORR reaction pathway mainly depends on the catalyst surface's initial oxygen dissociation energy barrier [56–58]. In addition, the ORR synergist action relies upon the proclivity of the oxygen species for the impetus particles. In our work, surface Cu species had different oxidation states for ORR. Cu_2O was generally easy to oxidize to CuO, and thus bound oxygen, consistent with the characterization results in XPS above. Moreover, nanoscale Cu_2O could be uniformly dispersed on the electron-conducting carrier such as carbon, and the electrons could be continually provided to the oxygen, thereby improving the catalytic activity [31].

The stability of the catalyst is critical for its performance for fuel cells; therefore, we tested the stability of Cu@C-800 and Pt/C using the chronoamperometric method by comparing the normalized current (I/I_0) of Cu@C-800 with a commercial Pt/C catalyst

(Figure 5h). It was observed that Cu@C-800 showed better stability, as the normalized current remained at 86% after 30,000 s, which is attributed to the nano-sized Cu species with various valance, carbon rod as the carrier, and the mesoporous profile.

The methanol durability analysis is also shown in Figure 5i. In the typical experiment, 10 mL of methanol was injected in 600 s, and the current for the commercial Pt/C sample dropped sharply on the methanol injection. In contrast, the current density for Cu@C-800 was only lowered by 5%, compared with that of Pt/C, indicating that Cu@C-800 has superior tolerance to methanol.

3. Materials and Methods

3.1. Materials

All medicines are of analytical grade and are used without further purification. $Cu(NO_3)_2 \cdot 3H_2O$ was purchased from Macleans, NaOH, KOH, $C_7H_5NaO_3$, KCl was purchased from Aladdin, and $FeCl_3$ was purchased from Tianjin Beilian Fine Chemicals Development Co., Ltd located in Tianjin, China. All aqueous solutions used deionized water preparation.

3.2. Synthesis of Electrocatalysts

3.2.1. Synthesis of Cu(OH)(Hsal)·H2O Precursor

The precursor was prepared by a simple co-precipitation method. In a typical method, $Cu(NO_3)_2 \cdot 3H_2O$ (0.02 mol) and $C_7H_5O_3Na$ (0.04 mol) are mixed in 250 mL of deionized water, dissolved in a beaker, and poured into the deionized water in a three-necked flask to start stirring. In order to control the pH at 4,1 M NaOH solution was slowly dropped into the flask through the dropping funnel and stirred at 90 °C for 24 h. The precipitate was separated by centrifugation, washed repeatedly, and dried in a vacuum oven at 50 °C overnight.

3.2.2. Synthesis of Cu@C Nanofibers

Put the Cu(OH)(Hsal)·H2O precursor in the center of the porcelain boat in a tube furnace. In an argon atmosphere, the furnace temperature is increased at 5 °C min^{-1}, and then kept at 800 °C for 2 h. The sample is named Cu@C.

3.2.3. Synthesis of Cu/CuOx@C Nanofibers

Under the condition of controlling the pH to 2, configure 50 mL of 0.012 M $FeCl_3$ solution, and add 0.2 g of Cu@C nanofibers to it and stir for 30 min. The precipitate was separated by suction filtration, washed repeatedly, and dried under vacuum at 50 °C overnight. The sample is named Cu@C-etching. Put Cu@C-etching in a tube furnace, blow in argon gas, and heat up the furnace at 5 °C min^{-1} and keep it for 2 h for secondary pyrolysis to obtain Cu/CuOx@C. According to the secondary pyrolysis temperature, the samples are named Cu@C-600, Cu@C-700, Cu@C-800, Cu@C-900.

3.3. Characterization

A Bruker D8 Advance X-ray polycrystalline diffractometer (Bruker, Billerica, MA, USA) was also used to record the X-ray diffraction (XRD) spectra with a scanning range of 10°–80° and a scanning speed of 4° min^{-1}. The JEOL JSM-7100F scanning electron microscope (Japan Electron Optics Laboratory, Tokyo Akishima Station, Japan) was also used to analyze the particles and morphology of the catalyst, and the material was analyzed by energy dispersive X-ray spectroscopy (EDX) at an accelerating voltage of 200 kV. The FEI Talos-S transmission electron microscope (Frequency Electronics, Inc., Columbia, MD, USA) was used to analyze the particle size and morphology of the catalyst. Raman spectroscopy was detected at 514 nm using Horiba Scientific LabRAM HR Evolution Raman spectrometer (HORIBA Scientific, Palaiseau, France). The infrared spectrum was obtained by Bruker TENSOR 27 infrared spectrometer (Bruker, Billerica, MA, USA). The model of the automatic specific surface and porosity analyzer is Mike 2460 (Micromeritics, Atlanta, GA, USA). We

also used X-ray photoelectron spectroscopy analyzer Thermo Scientific ESCALAB 250Xi (Thermo Scientific, Thermo Scientific, Waltham, MA, USA) to analyze elements.

3.4. Electrochemistry

All electrochemical tests are performed on the IVIUM instrument (Lvium Technologies BV, Eindhoven, Netherlands) at 25 °C. The electrolytic cell uses a traditional five-port electrolytic cell with an electrolyte of 0.1 M KOH. A platinum wire and Ag/AgCl electrode are used as the counter electrode and the reference electrode, and the salt bridge uses a saturated KCl solution. The working electrode is a rotating disk electrode (RDE), and the electrode is a 5 mm glass-carbon disk. Disperse 5 mg of catalyst in 1 ml of water:ethanol = 1:9 solution and add 7 μL of 5 wt% Nafion, then sonicate it in a cell pulverizer for 8 min to prepare ink. Take a 10 μL ink drop and apply it on the surface of the electrode. The linear sweep volt-ampere (LSV) curve is 0.2–1.2 V (vs. RHE), and the sweep rate is 5 mv s^{-1}.

The conversion of Ag/AgCl electrode and standard hydrogen electrode is as follows:

$$V_{RHE} = V_{Ag/AgCl} + 0.059pH + 0.197 \tag{1}$$

The *Koutecky-Levich* (*K-L*) equation is used to calculate the number of electrons transferred in the ORR process. Obtain the LSV curves of the relevant catalysts at 400, 625, 900, 1225, 1600 rpm. Based on these curves, calculate the electron transfer number (N) of each oxygen molecule involved in the ORR process according to the *Koutecky-Levich* (*K-L*) equation as follows:

$$\frac{1}{J} = \frac{1}{J_K} + \frac{1}{B\omega^{0.5}} \tag{2}$$

where *J* is the current density, J_K is the dynamic current density, ω is the rotation rate of the electrode, and *B* can be obtained from the *K-L* diagram using Equation (2). The value of n can be calculated from the slope of the linear curve based on the following relationship:

$$B = 0.62nF(D_{O2})^{2/3}v^{-1/6}C_{O2} \tag{3}$$

In Equation (3), *F* in *F* is the Faraday constant (96485 C mol^{-1}), is the diffusion coefficient of O_2 in 0.1 M KOH electrolyte (1.9×10^{-5} cm^2 s^{-1}), and *v* is the dynamic viscosity (0.01 cm^2 s^{-1}), is the saturation concentration of O (1.2×10^{-6} mol cm^{-3}). The value of *n* represents the number of electrons transferred during the ORR process.

4. Conclusions

We synthesized carbon-coated copper nanoparticles on carbon nanofibers and finally prepared Cu/CuO$_x$@C composites through an etching-pyrolysis process, and the prepared material shows excellent ORR performance (E_{onset} = 1.00 V vs. RHE, $E_{1/2}$ = 0.81 V vs. RHE, J_L = 5.15 mA cm^{-2}, Tafel slope = 107 mV dec^{-1}). As the uniform 1D permeable design gives a higher surface region, the rich Cu nano-species on the material's surface and the high electrical conductivity have laid the foundation for excellent catalytic activity. Due to the nature of the Cu-based material and the reduction in the proportion of C–OH groups, it has a higher selectivity for the four-electron process and is superior to platinum carbon in its resistance to methanol. Such copper-based electrocatalysts will likely supplant some costly platinum-based materials in electrochemically energy conversion applications.

electron transfer numbers at 0.2, 0.3, 0.4 and 0.5 V; Figure S9: Cu@C-800 material surface (a) Simulation of ORR process (b) $4e^-$ process. Table S1: Cu@C-(600,700,800,900) Cu(111) XRD half-value width, particle size, O's XPS fine spectrum peak area and the ratio of C–OH, O–Cu, Cu's XPS fine spectrum Peak area and the ratio of Cu(0)+Cu(I), Cu(II); Table S2: compares the ORR activity of Cu@C-800 and Cu-based catalysts. References [59–65] are cited in the Supplementary Materials.

Author Contributions: Conceptualization, D.Z. and L.C.; methodology, D.Z.; software, Y.-F.L.; validation, D.Z., L.C., and Q.Y.; formal analysis, D.Z.; investigation, D.Z.; resources, D.Z.; data curation, L.-X.L.; writing—original draft preparation, L.D.; writing—review and editing, D.Z.; visualization, Z.-L.R.; supervision, S.-D.X. and H.-J.G.; project administration, L.-J.S. and Y.H.; funding acquisition, Q.Y. All authors have read and agreed to the published version of the manuscript.

Data Availability Statement: Data are available within the article.

Conflicts of Interest: The authors declare no conflict of interest.

References

1. Lewis, N.; Nocera, D. Powering the planet chemical challenges in solar energy utilization. *Proc. Natl. Acad. Sci. USA* **2006**, *103*, 15729–15735. [CrossRef] [PubMed]
2. Xu, X.; Shao, Z.; Jiang, S.P. High-Entropy Materials for Water Electrolysis. *Energy Technol.* **2022**, *10*, 1–17. [CrossRef]
3. Hamrock, S.; Herring, A.; Zawodzinski, T. Fuel Cell Chemistry and Operation. *ACS Symposium.* **2010**, *172*, 1. [CrossRef]
4. Xu, X.; Su, C.; Shao, Z. Fundamental Understanding and Application of $Ba_{0.5}Sr_{0.5}Co_{0.8}Fe_{0.2}O_3-\delta$Perovskite in Energy Storage and Conversion: Past, Present, and Future. *Energy Fuels.* **2021**, *35*, 13585–13609. [CrossRef]
5. Sumboja, A.; Ge, X.; Goh, T.; Li, B.; Geng, D.; Hor, T.; Zong, Y.; Liu, Z. Manganese Oxide Catalyst Grown on Carbon Paper as an Air Cathode for High-Performance Rechargeable Zinc-Air Batteries. *ChemPlusChem* **2015**, *80*, 1341–1346. [CrossRef] [PubMed]
6. Huang, L.; Zaman, S.; Tian, X.; Wang, Z.; Fang, W.; Xia, B. Advanced Platinum-Based Oxygen Reduction Electrocatalysts for Fuel Cells. *Accounts Chem. Res.* **2021**, *54*, 311–322. [CrossRef]
7. Yang, L.; Shui, J.; Du, L.; Shao, Y.; Liu, J.; Dai, L.; Hu, Z. Carbon-Based Metal-Free ORR Electrocatalysts for Fuel Cells: Past, Present, and Future. *Adv. Mater.* **2019**, *31*, 1804799. [CrossRef]
8. Paul, R.; Du, F.; Dai, L.; Ding, Y.; Wang, Z.; Wei, F.; Roy, A. 3D Heteroatom-Doped Carbon Nanomaterials as Multifunctional Metal-Free Catalysts for Integrated Energy Devices. *Adv. Mater.* **2019**, *31*, 1805598. [CrossRef]
9. Liang, Y.; Li, Y.; Wang, H.; Zhou, J.; Wang, J.; Regier, T.; Dai, H. Co_3O_4 nanocrystals on graphene as a synergistic catalyst for oxygen reduction reaction. *Nat. Mater.* **2011**, *10*, 780–786. [CrossRef]
10. Chen, G.; Liu, P.; Liao, Z.; Sun, F.; He, Y.; Zhong, H.; Zhang, T.; Zschech, E.; Chen, M.; Wu, G.; et al. Zinc-Mediated Template Synthesis of Fe-N-C Electrocatalysts with Densely Accessible Fe-N_x Active Sites for Efficient Oxygen Reduction. *Adv. Mater.* **2020**, *32*, 1907399. [CrossRef]
11. Zhang, X.; Xu, X.; Yao, S.; Hao, C.; Pan, C.; Xiang, X.; Tian, Z.; Shen, P.; Shao, Z.; Jiang, S.; et al. Boosting Electrocatalytic Activity of Single Atom Catalysts Supported on Nitrogen-Doped Carbon through N Coordination Environment Engineering. *Small* **2022**, *18*, 2105329. [CrossRef] [PubMed]
12. Zhu, Z.; Yin, H.; Wang, Y.; Chuang, C.; Xing, L.; Dong, M.; Lu, Y.; Casillas, G.; Zheng, Y.; Chen, S.; et al. Coexisting Single-Atomic Fe and Ni Sites on Hierarchically Ordered Porous Carbon as a Highly Efficient ORR Electrocatalyst. *Adv. Mater.* **2020**, *32*, 2004670. [CrossRef] [PubMed]
13. Peng, H.; Liu, F.; Liu, X.; Liao, S.; You, C.; Tian, X.; Nan, H.; Luo, F.; Song, H.; Fu, Z.; et al. Effect of Transition Metals on the Structure and Performance of the Doped Carbon Catalysts Derived From Polyaniline and Melamine for ORR Application. *ACS Catal.* **2014**, *4*, 3797–3805. [CrossRef]
14. Yang, L.; Cheng, D.; Xu, H.; Zeng, X.; Wan, X.; Shui, J.; Xiang, Z.; Cao, D. Unveiling the high-activity origin of single-atom iron catalysts for oxygen reduction reaction. *Proc. Natl. Acad. Sci. USA* **2018**, *115*, 6626–6631. [CrossRef] [PubMed]
15. Yin, P.; Yao, T.; Wu, Y.; Zheng, L.; Lin, Y.; Liu, W.; Ju, H.; Zhu, J.; Hong, X.; Deng, Z.; et al. Single Cobalt Atoms with Precise N-Coordination as Superior Oxygen Reduction Reaction Catalysts. *Angew. Chem.* **2016**, *128*, 10958–10963. [CrossRef]
16. Xiong, Y.; Yang, Y.; Disalvo, F.J.; Abruna, H.D. Metal-Organic-Framework-Derived Co-Fe Bimetallic Oxygen Reduction Electrocatalysts for Alkaline Fuel Cells. *J. Am. Chem. Soc.* **2019**, *141*, 10744–10750. [CrossRef]
17. Wang, J.; Liu, W.; Luo, G.; Li, Z.; Zhao, C.; Zhang, H.; Zhu, M.; Xu, Q.; Wang, X.; Zhao, C.; et al. Synergistic effect of well-defined dual sites boosting the oxygen reduction reaction. *Energ. Environ. Sci.* **2019**, *11*, 3375–3379. [CrossRef]
18. Chen, Y.; Gao, R.; Ji, S.; Li, H.; Tang, K.; Jiang, P.; Hu, H.; Zhang, Z.; Hao, H.; Qu, Q.; et al. Atomic-Level Modulation of Electronic Density at Cobalt Single-Atom Sites Derived from Metal-Organic Frameworks: Enhanced Oxygen Reduction Performance. *Angew. Chem. Int. Edit.* **2022**, *61*, 3212–3221. [CrossRef]

19.　Wang, X.; Jia, Y.; Mao, X.; Liu, D.; He, W.; Li, J.; Liu, J.; Yan, R.; Chen, J.; Song, L.; et al. Edge-Rich FeN$_4$ Active Sites in Defective Carbon for Oxygen Reduction Catalysis. *Adv. Mater.* **2020**, *32*, 2000966. [CrossRef]

20.　Shao, Y.; Dodelet, J.P.; Wu, G.; Zelenay, P. PGM-Free Cathode Catalysts for PEM Fuel Cells: A Mini-Review on Stability Challenges. *Adv. Mater.* **2019**, *31*, 1807615. [CrossRef]

21.　Li, J.; Chen, M.; Cullen, D.A.; Hwang, S.; Wang, M.; Li, B.; Liu, K.; Karakalos, S.; Lucero, M.; Zhang, H.; et al. Atomically dispersed manganese catalysts for oxygen reduction in proton-exchange membrane fuel cells. *Nat. Catal.* **2018**, *1*, 935–945. [CrossRef]

22.　Yu, H.; Fisher, A.C.; Cheng, D.; Cao, D. Cu, N-codoped Hierarchical Porous Carbons as Electrocatalysts for Oxygen Reduction Reaction. *ACS App. Mater. Inter.* **2016**, *8*, 21431–21439. [CrossRef] [PubMed]

23.　Tong, M.; Sun, F.; Xie, Y.; Wang, Y.; Yang, Y.; Tian, C.; Wang, L.; Fu, H. Operando Cooperated Catalytic Mechanism of Atomically Dispersed Cu-N$_4$ and Zn-N$_4$ for Promoting Oxygen Reduction Reaction. *Angew. Chem.* **2021**, *133*, 14124–14131. [CrossRef]

24.　Shang, H.; Zhou, X.; Dong, J.; Li, A.; Zhao, X.; Liu, Q.; Lin, Y.; Pei, J.; Li, Z.; Jiang, Z.; et al. Engineering unsymmetrically coordinated Cu-S$_1$N$_3$ single atom sites with enhanced oxygen reduction activity. *Nat. Commun.* **2020**, *11*, 3049. [CrossRef] [PubMed]

25.　Kuang, M.; Wang, Q.; Han, P.; Zheng, G. Cu, Co-Embedded N-Enriched Mesoporous Carbon for Efficient Oxygen Reduction and Hydrogen Evolution Reactions. *Adv. Energy Mater.* **2017**, *7*, 1700193. [CrossRef]

26.　Yan, X.; Tong, X.; Zhang, Y.; Han, X.; Wang, Y.; Jin, G.; Qin, Y.; Guo, X. Cuprous oxide nanoparticles dispersed on reduced graphene oxide as an efficient electrocatalyst for oxygen reduction reaction. *Chem. Commun.* **2012**, *48*, 1892–1894. [CrossRef] [PubMed]

27.　Zhang, T.; Cheng, R.; Li, B.; Wang, C.; Guo, Y.; Liu, J.; Wang, L. Novel one-dimensional Cu@C nanofibers: Direct solid-state synthesis and applications in electrocatalytic water splitting. *Chem. Commun.* **2021**, *57*, 769–772. [CrossRef]

28.　Dai, L.; Qin, Q.; Wang, P.; Zhao, X.; Hu, C.; Liu, P.; Qin, R.; Chen, M.; Ou, D.; Xu, C.; et al. Ultrastable atomic copper nanosheets for selective electrochemical reduction of carbon dioxide. *Sci. Adv.* **2017**, *3*, 1701069. [CrossRef]

29.　Xie, Y.; Li, C.; Castillo, E.; Fang, J.; Dimitrov, N. Nanoporous Pd-Cu Thin Films as Highly Active and Durable Catalysts for Oxygen Reduction in Alkaline Media. *Electrochim. Acta* **2021**, *385*, 138306. [CrossRef]

30.　Yang, L.; Liu, D.; Cui, G.; Xie, Y. Cu$_{2+1}$O/graphene nanosheets supported on three dimensional copper foam for sensitive and efficient non-enzymatic detection of glucose. *RSC Adv.* **2017**, *7*, 19312–19317. [CrossRef]

31.　Cao, X.; Cui, L.; Liu, B.; Liu, Y.; Jia, D.; Yang, W.; Razal, J.M.; Liu, J. Reverse synthesis of star anise-like cobalt doped Cu-MOF/Cu$_{2+1}$O hybrid materials based on a Cu(OH)$_2$ precursor for high performance supercapacitors. *J. Mater. Chem. A* **2019**, *7*, 3815–3827. [CrossRef]

32.　Wan, C.; Duan, X.; Huang, Y. Molecular Design of Single-Atom Catalysts for Oxygen Reduction Reaction. *Adv. Energy Mater.* **2020**, *10*, 1903815. [CrossRef]

33.　Hong, J.; Jin, C.; Yuan, J.; Zhang, Z. Atomic Defects in Two-Dimensional Materials: From Single-Atom Spectroscopy to Functionalities in Opto-/Electronics, Nanomagnetism, and Catalysis. *Adv. Mater.* **2017**, *29*, 1606434. [CrossRef]

34.　Shi, Z.; Sun, G.; Yuan, R.; Chen, W.; Wang, Z.; Zhang, L.; Zhan, K.; Zhu, M.; Yang, J.; Zhao, B. Scalable fabrication of NiCo$_2$O$_4$/reduced graphene oxide composites by ultrasonic spray as binder-free electrodes for supercapacitors with ultra-long lifetime. *J. Mater. Sci. Technol.* **2022**, *99*, 260–269. [CrossRef]

35.　Zhang, Y.; Li, P.; Yin, X.; Yan, Y.; Zhan, K.; Yang, J.; Zhao, B. Cobalt sulfide supported on nitrogen and sulfur dual-doped reduced graphene oxide for highly active oxygen reduction reaction. *RSC Adv.* **2017**, *7*, 5024. [CrossRef]

36.　Zhao, Y.; Chen, Z.; Xiong, D.; Qiao, Y.; Tang, Y.; Gao, F. Hybridized phosphate with ultrathin nanoslices and single crystal microplatelets for high performance supercapacitors. *SCI. REP-UK* **2016**, *6*, 17613. [CrossRef]

37.　Reichardt, W.; Gompf, F.; Aïn, M.; Wanklyn, B.M. Lattice dynamics of cupric oxide. *Zeitschrift für Physik B Condensed Matter* **1990**, *81*, 19–24. [CrossRef]

38.　Chen, X.; Irwin, J.C.; Franck, J.P. Evidence for a strong spin-phonon interaction in cupric oxide. *Phys. Rev. B* **1995**, *52*, 13130–13133. [CrossRef]

39.　Kliche, G.; Popovic, Z. Far-infrared spectroscopic investigations on CuO. *Phys. Rev. B* **1991**, *42*, 10060–10066. [CrossRef]

40.　Debbichi, L.; Lucas, M.C.M.D.; Pierson, J.F.; Krüger, P. Vibrational Properties of CuO and Cu$_4$O$_3$ from First-Principles Calculations, and Raman and Infrared Spectroscopy. *J. Phys. Chem. C* **2012**, *116*, 10232–10237. [CrossRef]

41.　Petroff, Y.; Yu, P.Y.; Shen, Y.R. Study of photoluminescence in Cu$_2$O. *Phys. Rev. B* **1975**, *12*, 2488–2495. [CrossRef]

42.　Ivanda, M.; Waasmaier, D.; Endriss, A. Low-temperature anomalies of cuprite observed by Raman spectroscopy and x-ray powder diffraction. *J. Raman. Spectrosc.* **1997**, *28*, 487–493. [CrossRef]

43.　Guo, Y.; Dai, M.; Zhu, Z.; Chen, Y.; He, H.; Qin, T. Chitosan modified Cu$_2$O nanoparticles with high catalytic activity for p-nitrophenol reduction. *Appl. Surf. Sci.* **2019**, *480*, 601–610. [CrossRef]

44.　Guo, D.; Wang, L.; Du, Y.; Ma, Z.; Shen, L. Preparation of octahedral Cu$_2$O nanoparticles by a green route. *Mater. Lett.* **2015**, *160*, 541–543. [CrossRef]

45.　Sahoo, R.; Dutta, S.; Pradhan, M.; Ray, C.; Roy, A.; Pal, T.; Pal, A. Arsenate stabilized Cu$_2$O nanoparticle catalyst for one-electron transfer reversible reaction. *Dalton Trans.* **2014**, *43*, 6677–6683. [CrossRef]

46.　Biesinger, M.C. Advanced analysis of copper X-ray photoelectron spectra. *Surf. Interface. Anal.* **2017**, *49*, 1325–1334. [CrossRef]

47.　Tran, D.T.; Le, H.T.; Doan, T.L.L.; Kim, N.H.; Lee, J.H. Pt Nanodots Monolayer Modified Mesoporous Cu@Cu$_x$O Nanowires for Improved Overall Water Splitting Reactivity. *Nano Energy* **2019**, *59*, 216–228. [CrossRef]

48. He, H.; Wang, M.; Zhao, J.; Zhang, Y. Poly (10,12-bis(4-hexylthiophen-2-yl)thieno[3′,4′:5,6]pyrazino[2,3-f][1,10]-phenanthroline)-copper(II) complex as an efficient electrocatalyst for oxygen reduction. *Chem. Eng. J.* **2017**, *316*, 680–691. [CrossRef]

49. Wang, F.; Zhao, Y.; Wei, P.; Zhang, Q.; Liu, J. Efficient electrocatalytic O_2 reduction at copper complexes grafted onto polyvinylimidazole coated carbon nanotubes. *Chem. Commun.* **2017**, *53*, 1514–1517. [CrossRef]

50. Yang, L.; Yu, J.; Wei, Z.; Li, G.; Cao, L.; Zhou, W.; Chen, S. Co-N-doped MoO_2 Nanowires as Efficient Electrocatalysts for the Oxygen Reduction Reaction and Hydrogen Evolution Reaction. *Nano Energy* **2017**, *41*, 772–779. [CrossRef]

51. Ferrero, G.A.; Preuss, K.; Marinovic, A.; Jorge, A.B.; Mansor, N.; Brett, D.J.L.; Fuertes, A.B.; Sevilla, M.; Titirici, M. Fe-N-Doped Carbon Capsules with Outstanding Electrochemical Performance and Stability for the Oxygen Reduction Reaction in Both Acid and Alkaline Conditions. *ACS Nano* **2016**, *10*, 5922–5932. [CrossRef] [PubMed]

52. Li, W.; Min, C.; Tan, F.; Li, Z.; Zhang, B.; Si, R.; Xu, M.; Liu, W.; Zhou, L.; Wei, Q.; et al. Bottom-Up Construction of Active Sites in a Cu-N_4-C Catalyst for Highly Efficient Oxygen Reduction Reaction. *ACS Nano* **2019**, *13*, 3177–3187. [CrossRef] [PubMed]

53. Sun, T.; Li, Y.; Cui, T.; Xu, L.; Wang, Y.; Chen, W.; Zhang, P.; Zheng, T.; Fu, X.; Zhang, S.; et al. Engineering of Coordination Environment and Multiscale Structure in Single-Site Copper Catalyst for Superior Electrocatalytic Oxygen Reduction. *Nano Lett.* **2020**, *20*, 6206–6214. [CrossRef] [PubMed]

54. Zhang, Z.; Sun, W.; Shang, H.; Chen, W.; Sun, T.; Li, H.; Dong, J.; Zhou, J.; Li, Z.; Wang, Y.; et al. Atomic interface effect of a single atom copper catalyst for enhanced oxygen reduction reactions. *Energ. Environ. Sci.* **2019**, *12*, 3508–3514. [CrossRef]

55. Zhang, T.; Zhang, B.; Peng, Q.; Zhou, J.; Sun, Z. Mo_2 B_2 MBene-supported single-atom catalysts as bifunctional HER/OER and OER/ORR electrocatalysts. *J. Mater. Chem. A* **2021**, *9*, 433–441. [CrossRef]

56. Nilekar, A.U.; Mavrikakis, M. Improved oxygen reduction reactivity of platinum monolayers on transition metal surfaces. *Surf. Sci.* **2008**, *602*, 89–94. [CrossRef]

57. Qiu, C.; Wang, S.; Zuo, J.; Zhang, B. Photocatalytic CO_2 Reduction Coupled with Alcohol Oxidation over Porous Carbon Nitride. *Catalysts* **2022**, *12*, 672. [CrossRef]

58. Zhang, B.; Qiu, C.; Wang, S.; Gao, H.; Yu, K.; Zhang, Z.; Ling, X.; Ou, W.; Su, C. Electrocatalytic water-splitting for the controllable and sustainable synthesis of deuterated chemicals. *Sci. Bull.* **2021**, *66*, 562–569. [CrossRef]

59. Li, P.; Jin, Z.; Qian, Y.; Fang, Z.; Xiao, D.; Yu, G. Supramolecular confinement of single Cu atoms in hydrogel frameworks for oxygen reduction electrocatalysis with high atom utilization. *Mater. Today.* **2020**, *35*, 78–86. [CrossRef]

60. Meng, Y.; Yin, J.; Jiao, T.; Bai, J.; Zhang, L.; Su, J.; Liu, S.; Bai, Z.; Cao, M.; Peng, Q. Self-assembled copper/cobalt-containing polypyrrole hydrogels for highly efficient ORR electrocatalysts. *J. Mol. Liq.* **2019**, *298*, 112010. [CrossRef]

61. Xie, Y.; Zhang, C.; He, X.; Su, J.W.; Parker, T.; White, T.A.; Griep, M.H.; Lin, J. Copper-promoted nitrogen-doped carbon derived from zeolitic imidazole frameworks for oxygen reduction reaction. *Appl. Surf. Sci.* **2019**, *464*, 344–350. [CrossRef]

62. Yang, Y.; Wang, C.; Gao, S.; Mao, K.; Xia, G.; Lin, Z.; Jiang, P.; Hu, L.; Chen, Q. Incorporation of Cu-Nx cofactors into graphene encapsulated Co as biomimetic electrocatalysts for efficient oxygen reduction. *Nanoscale.* **2018**, *10*, 21076–21086. [CrossRef] [PubMed]

63. Wang, Z.; Jin, H.; Meng, T.; Liao, K.; Meng, W.; Yang, J.; He, D.; Xiong, Y.; Mu, S. Fe, Cu-Coordinated ZIF-Derived Carbon Framework for Efficient Oxygen Reduction Reaction and Zinc-Air Batteries. *Adv. Funct. Mater.* **2018**, *28*, 1802596. [CrossRef]

64. Saianand, G.; Gopalan, A.; Lee, J.C.; Sathish, C.I.; Gopalakrishnan, K.; Unni, G.; Shanbhag, D.; Dasireddy, V.D.B.C.; Yi, J.; Xi, S.; et al. Mixed Copper/Copper-Oxide Anchored Mesoporous Fullerene Nanohybrids as Superior Electrocatalysts toward Oxygen Reduction Reaction. *Small* **2020**, *16*, 1903937. [CrossRef] [PubMed]

65. Wang, T.; Yang, R.; Shi, N.; Yang, J.; Yan, H.; Wang, J.; Ding, Z.; Huang, W.; Luo, Q.; Lin, Y.; et al. Cu, N-Codoped Carbon Nanodisks with Biomimic Stomata-Like Interconnected Hierarchical Porous Topology as Efficient Electrocatalyst for Oxygen Reduction Reaction. *Small* **2019**, *15*, 1902410. [CrossRef]